Comput Geosci (2013) 17:67–81
DOI 10.1007/s10596-012-9314-2

ORIGINAL PAPER

A network flow model for the genesis and migration of gas phase

Koukung Alex Chang · W. Brent Lindquist

Received: 13 June 2011 / Accepted: 20 August 2012 / Published online: 14 September 2012

Abstract We present a network flow model to compute transport, through a pore network, of a compositional fluid consisting of water with a dissolved hydrocarbon gas. The model captures single-phase flow (below local bubble point conditions) as well as the genesis and migration of the gas phase when bubble point conditions are achieved locally. Constant temperature computational tests were run on simulated 2D and 3D micro-networks near bubble point pressure conditions. In the 2D simulations which employed a homogeneous network, negligible capillary pressure, and linear relative permeability relations, the observed concentration of CO_2 dissolved in the liquid phase throughout the medium was linearly related to the liquid pressure. In the case of no gravity, the saturation of the gas phase throughout the medium was also linearly related to the liquid pressure; under gravity, the relationship became nonlinear in regions where buoyancy forces were significant. The 3D heterogeneous network model had nonnegligible capillary pressure and nonlinear relative permeability functions. While 100 % of the CO_2 entered the 3D network dissolved in the liquid phase, 25 % of the void space was occupied by gas phase and 47 % of the CO_2 exiting the outlet face did so via the gaseous phase after 500 s of simulation time.

K. A. Chang (✉)
Department of Applied Mathematics, National Pingtung University of Education, Pingtung, Taiwan, 90003 Republic of China
e-mail: chang@mail.npue.edu.tw

W. B. Lindquist
Department of Applied Mathematics and Statistics, Stony Brook University, Stony Brook, NY 11794-3600, USA
e-mail: b.lindquist@stonybrook.edu

Keywords Network flow model · Gas genesis · Carbon dioxide sequestration · Compositional flow

Mathematics Subject Classifications (2010) 65C20 · 68U20 · 76Q05 · 76S05 · 76T10

1 Introduction

Injection of supercritical CO_2 into a formation containing saline water results in dynamic two-phase flow, with the phases separated by a moving front. Behind the front, a CO_2-saturated aqueous phase remains, which can migrate over slower time scales. The reactive capabilities of this CO_2-saturated brine phase are of great concern to sequestration technology. Simulations using network flow models [26, 30–32] indicate that, due to the natural heterogeneities in porous media, bulk reaction rates are much slower in situ than predicted by laboratory-determined rate laws. In addition, if this saturated brine phase migrates into regions where pressures fall below bubble point conditions, a gas phase will form. The production of a gas phase has the potential to reduce reaction rates even further by limiting the available volume of reactive fluid and/or by impeding the motion of the brine phase.

Independent of reactive effects, the genesis and migration of gas formation produces its own potential risk factors. Anthropogenic emissions of carbon dioxide have contributed to rising mean global temperatures [3, 15, 44]. With a maximum worldwide CO_2 storage capacity estimated at 10^4–$2{\cdot}10^5$ Gt CO_2 [10], sequestration of CO_2 in deep saline aquifers is now a heavily researched strategy to reduce atmospheric CO_2 emissions [4–7, 14, 20, 23, 24, 35]. The potential to store

massive amounts of subsurface CO_2 must be evaluated relative to the potential risks of gas phase production and release. A massive release of a gas phase can be hazardous; more than 1,700 people were killed due to a sudden CO_2 eruption from Lake Nyos in Cameroon in 1986 [18, 27].

Field experiments, which are expensive in both time and money, are being augmented by an extensive arsenal of laboratory experiment, numerical simulation (e.g., [12]), and semi-analytic approaches (e.g., [33]) to increase our understanding of sequestration. The simulations depend on adequate geochemical models in order to understand the mechanisms that govern the chemical reaction, transport, and transformation of the injected CO_2 over different length and time scales. There are a number of oil industry standard codes (e.g., Eclipse [38, 39]) capable of performing compositional (phase change) simulations at the field scale. Our interest is to develop such simulation capability at the pore scale with twin goals of understanding pore level detail as well as computing bulk behavior at the core scale.

At the pore scale, network models have been used extensively to investigate (1) single and multiphase flow [1, 8, 11, 13, 16, 19, 21, 22, 25, 28, 34, 36, 40] including determination of absolute and relative permeability [9, 29, 41, 42], (2) specific studies of bubble transport [43] and recently, (3) reactive flow [26, 30] relevant to geological sequestration of CO_2. Network models have not, as yet, addressed the modeling of phase creation and subsequent transport. In this paper, we develop a network model with which to investigate the genesis and migration of a gas phase. The mathematical model is described in Section 2; the numerical algorithm is formulated in Section 3; and the results of 2D and 3D computational tests are presented in Section 4. Final discussion is presented in Section 5.

2 The mathematical model

The model contains two main components: fluid transport equations which follow from conservation of mass for each species and phase equilibrium conditions for the liquid and gas phases.

2.1 Mass conservation

In this model, liquid and gas phases involving two chemical species, H_2O and CO_2, are considered. Let s_l be the saturation of the liquid phase and s_g be the saturation of the gaseous phase. By definition,

$$s_l + s_g = 1. \tag{1}$$

We assume that the liquid phase remains incompressible, with H_2O being the dominant species in the liquid phase. Therefore, the concentration of water in the liquid phase, $C_{H_2O;l}$, is always $C_{H_2O;l} = C_W$, where $C_W = 1/18$ mol cm^{-3} is the concentration of liquid water. Let $C_{H_2O;g}$, $C_{CO_2;l}$, and $C_{CO_2;g}$ denote the concentrations, respectively, of H_2O in the gaseous phase, CO_2 in the liquid phase, and CO_2 in the gaseous phase. The total molar concentrations of water, m_{H_2O}, and carbon dioxide, m_{CO_2}, are defined as

$$\begin{aligned} m_{H_2O} &= (s_l C_{H_2O;l} + s_g C_{H_2O;g}) \quad \text{and} \\ m_{CO_2} &= (s_l C_{CO_2;l} + s_g C_{CO_2;g}). \end{aligned} \tag{2}$$

Conservation of mass of individual species asserts that, applied to each individual pore,

$$\begin{aligned} V\frac{d(m_{H_2O})}{dt} &= [Q_l C_{H_2O;l} + Q_g C_{H_2O;g}]_{in} \\ &\quad - [Q_l C_{H_2O;l} + Q_g C_{H_2O;g}]_{out} + S_{H_2O}, \end{aligned} \tag{3}$$

and

$$\begin{aligned} V\frac{d(m_{CO_2})}{dt} &= [Q_l C_{CO_2;l} + Q_g C_{CO_2;g}]_{in} \\ &\quad - [Q_l C_{CO_2;l} + Q_g C_{CO_2;g}]_{out} + S_{CO_2}, \end{aligned} \tag{4}$$

where V is the volume of the pore, Q_l and Q_g denote the liquid and gas volumetric flow rates (cm^3 s^{-1}), $[\cdot]_{in}$ and $[\cdot]_{out}$ correspond to the total mass change rates (mol s^{-1}) at the inflow and outflow boundaries of the pore, and S_{H_2O} and S_{CO_2} are respective mass rate (mol s^{-1}) source terms. The flow rates Q_l and Q_g through an individual channel are given by

$$Q_p = -\Lambda_p \Delta(P_p - \rho_p G z), \quad p = l, g, \tag{5}$$

where Λ_p is the channel conductivity of phase p; ρ_p and P_p are the density and pressure of phase p; G is the gravitational constant; and z is vertical position. A buoyancy force is described implicitly in the model. The gas phase flow rate can be reexpressed as

$$Q_g = -\Lambda_g \Delta[(P_g - \rho_l G z) + (\rho_l G z - \rho_g G z)]. \tag{6}$$

The last term explicitly expresses the buoyancy forces, which will dominate at low flow rates ($P_g - \rho_l G z \sim 0$).

The density of each phase is modeled to change with dissolved CO_2,

$$\rho_p = 18.015 C_{H_2O;p} + 44.098 C_{CO_2;p}, \quad p = l, g, \tag{7}$$

where 18.015 and 44.098 are (to five significant digits) the respective molecular weights of water and carbon dioxide.

For later use, we note that for steady-state, axisymmetric, single phase flow of an incompressible fluid of viscosity ν, the volumetric flow rate Q through a

channel of constant circular cross section is given by the Hagen–Poiseuille equation,

$$Q = \frac{\pi r^4}{8\nu}\frac{|\Delta P|}{L}, \tag{8}$$

where r and L are the radius and length of the channel, respectively, and ΔP is the pressure drop in the flow direction. Equation 8 identifies the fluid conductivity of a circular channel as $\Lambda = (\pi r^4)/8\nu L$. Identifying $A = \pi r^2$ as the cross-sectional area of the channel, $\kappa = r^2/8$ can be interpreted as an intrinsic permeability of a circular channel.

2.2 Phase pressure, partial pressure, and chemical potential equilibrium

At equilibrium, the pressure difference between the gas and liquid phases satisfies

$$P_g = P_l + P^c, \tag{9}$$

where P^c is the capillary pressure, and we have assumed the liquid phase to be the wetting phase. Assuming perfect wetting, the capillary pressure is given by the Young–Laplace equation,

$$P^c = 2\gamma/r, \tag{10}$$

where γ is the surface tension and r is the radius of curvature of the gas bubble. The surface tension is evaluated by the Eötvös rule,

$$\gamma V_W^{2/3} = k(T_c - T), \tag{11}$$

where $V_W = 18$ ml mol^{-1} is the molar volume of water, $T_c = 374$ °C is the critical temperature for water and $k = 2.1{\cdot}10^{-7}$ J K^{-1} mol$^{-2/3}$ is a constant. Evaluation of P^c requires an estimate for r. With V being the volume of a pore then $s_g V$ is the volume of the gas in the pore. As our network model employs spherical pores, the radius of curvature, r, of a gas bubble will not exceed $(3s_g V/4k)^{1/3}$. While we compute s_g for each pore, our model does not distinguish individual gas bubbles in any pore; therefore, we compute P^c using the estimate $r = (3s_g V/4k)^{1/3}$.

Compared to the rate at which the liquid phase typically flows through a geologic porous medium, the rate of CO_2 dissolving in, or escaping from, water is fast. Therefore, the model assumes that gas phase partial pressures remain in equilibrium while concentration changes take place.

The solubility of carbon dioxide in water depends on local pressure and temperature. At constant temperature, more CO_2 can be dissolved in water confined at higher pressure. For a pore network at constant temperature, if CO_2-saturated water from a higher pressure pore flows into a lower pressure pore, phase equilibrium requires some CO_2 to come out of solution, producing a gas bubble in the downstream pore.

The gas phase contains two species, CO_2 and water vapor. The total pressure of the gas phase is

$$P_g = P_{\mathrm{CO_2};g} + P_{\mathrm{H_2O};g}, \tag{12}$$

where $P_{\mathrm{CO_2};g}$ and $P_{\mathrm{H_2O};g}$ are partial pressures of CO_2 and H_2O in the gas phase, respectively. Our model assumes the gas phase is ideal; therefore, $P_{\mathrm{CO_2};g}$ and $P_{\mathrm{H_2O};g}$ follow the ideal gas law,

$$P_{\mathrm{CO_2};g} = C_{\mathrm{CO_2};g}RT, \quad P_{\mathrm{H_2O};g} = C_{\mathrm{H_2O};g}RT, \tag{13}$$

where R is the gas constant.

Under equilibrium conditions between the liquid and gas phases, the chemical potential of CO_2 in the liquid phase is equal to that of CO_2 in the gas phase, i.e.,

$$\mu^{\ominus}_{\mathrm{CO_2};l} + RT\ln\left(\frac{C_{\mathrm{CO_2};l}}{C_{\mathrm{H_2O};l} + C_{\mathrm{CO_2};l}}\right) = \mu^{\ominus}_{\mathrm{CO_2};g} + RT\ln\left(\frac{C_{\mathrm{CO_2};g}RT}{P^*_{\mathrm{CO_2}}}\right), \tag{14}$$

where $\mu^{\ominus}_{\mathrm{CO_2};l} = -385.98$ kJ mol^{-1} and $\mu^{\ominus}_{\mathrm{CO_2};g} = -394.36$ kJ mol^{-1} are the chemical potentials of CO_2 in the liquid and gas phase, respectively, at standard conditions (298 K, 1 bar pressure [2]) and $P^*_{\mathrm{CO_2}} = 1$ bar. Similarly, the chemical potential of H_2O in the liquid phase is equal to that of H_2O in the gas phase,

$$\mu^{\ominus}_{\mathrm{H_2O};l} + RT\ln\left(\frac{C_{\mathrm{H_2O};l}}{C_{\mathrm{H_2O};l} + C_{\mathrm{CO_2};l}}\right) = \mu^{\ominus}_{\mathrm{H_2O};g} + RT\ln\left(\frac{C_{\mathrm{H_2O};g}RT}{P^*_{\mathrm{H_2O}}}\right), \tag{15}$$

where $\mu^{\ominus}_{\mathrm{H_2O};l} = -273.13$ kJ mol^{-1} and $\mu^{\ominus}_{\mathrm{H_2O};g} = -228.57$ kJ mol^{-1}.

The model contains six unknowns, s_l, s_g, $C_{\mathrm{H_2O};g}$, $C_{\mathrm{CO_2};l}$, $C_{\mathrm{CO_2};g}$, and P_l and six equations, Eqs. 1, 3, 4, 14, 15, and 5, for Q_l. Solution of this nonlinear system is described in the next section.

3 Numerical model

The numerical model employs sequential solution for the pore pressures, saturations, and concentrations at each time step. The challenge in computing saturations and concentrations is to satisfy both mass conservation and phase equilibrium. This is done by updating species concentrations first due to transport followed

by a phase-change (flash) calculation for equilibrium concentrations and saturations in each pore.

3.1 Pressure solution

Update of the pressure solution assumes known phase and species concentrations in each pore. The pressure solution separates the pores into three categories—a pore either contains: (1) both liquid and gas phases; (2) liquid phase only, oversaturated with dissolved CO_2; or (3) liquid phase only, undersaturated with dissolved CO_2.

For a category 1 pore, under the assumption of phase equilibrium,

$$P_g = P_l + P^c = (C_{\mathrm{H_2O};g} + C_{\mathrm{CO_2};g})RT. \tag{16}$$

Let $C^{cr}_{\mathrm{CO_2};l}$ be the critical concentration of CO_2 that starts to generate a gas bubble in a pore of liquid pressure P_l. As shown in Appendix A,

$$C^{cr}_{\mathrm{CO_2};l} = \frac{[10^{-4}(P_l - P^0_w(T)) + 2\gamma]C_W}{10^{-4}(K_{\mathrm{CO_2}}(T) - P_l) - 2\gamma}. \tag{17}$$

For a category 2 pore ($C_{\mathrm{CO_2};l} > C^{cr}_{\mathrm{CO_2};l}$), the liquid phase pressure is evaluated as

$$P_l = P_g = P^0_w(T)\frac{C_{\mathrm{H_2O};l}}{C_{\mathrm{H_2O};l} + C_{\mathrm{CO_2}}} + K_{\mathrm{CO_2}}(T)\frac{C_{\mathrm{CO_2}}}{C_{\mathrm{H_2O};l} + C_{\mathrm{CO_2}}}, \tag{18}$$

as explained in Appendix B (where $C_{\mathrm{CO_2}}$ is defined).

Under the assumption that the liquid phase is incompressible, a category 3 pore satisfies the divergence free condition, $\nabla \cdot Q_l = 0$ which, applied to pore i in discrete form, is from Eq. 5,

$$\sum_{j=1}^{n} \Lambda_{ij}[(P_{l;i} - P_{l;j}) - \rho_l G(z_i - z_j)] = 0, \tag{19}$$

where: j indexes pores connected to i; n is the total number of pores connecting to i; Λ_{ij} is the conductivity of the liquid phase; $P_{l;i}$ and $P_{l;j}$ are the pressure of the liquid phase in pores i and j, respectively; and z_i, z_j are the z-coordinates of the two pores. The solution of the linear system of Eq. 19, employing, as boundary conditions, the pressure values at the inlet and outlet pores of the network and the (concentration determined) pressures for category 1 or 2 pores, provides values of P_l for all category 3 pores.

3.2 Transport update of concentrations

Assuming the source terms $S_{\mathrm{H_2O}}$ and $S_{\mathrm{CO_2}}$ are zero (no reactions), the first order difference approximations to Eqs. 3 and 4 are

$$V_i\frac{[m^{new}_{\mathrm{H_2O}}]_i - [m^{old}_{\mathrm{H_2O}}]_i}{\Delta t} = -\left(\sum_{Q_{l;ij}>0} Q_{l;ij}[C_{\mathrm{H_2O};l}]_i + \sum_{Q_{g;ij}>0} Q_{g;ij}[C_{\mathrm{H_2O};g}]_i + \sum_{Q_{l;ij}<0} Q_{l;ij}[C_{\mathrm{H_2O};l}]_j + \sum_{Q_{g;ij}<0} Q_{g;ij}[C_{\mathrm{H_2O};g}]_j\right) \tag{20}$$

and

$$V_i\frac{[m^{new}_{\mathrm{CO_2}}]_i - [m^{old}_{\mathrm{CO_2}}]_i}{\Delta t} = -\left(\sum_{Q_{l;ij}>0} Q_{l;ij}[C_{\mathrm{CO_2};l}]_i + \sum_{Q_{g;ij}>0} Q_{g;ij}[C_{\mathrm{CO_2};g}]_i + \sum_{Q_{l;ij}<0} Q_{l;ij}[C_{\mathrm{CO_2};l}]_j + \sum_{Q_{g;ij}<0} Q_{g;ij}[C_{\mathrm{CO_2};g}]_j\right), \tag{21}$$

where V_i is the volume of pore i; $[m^{new(old)}_\alpha]_i$ is the total molar concentration of species α in pore i at the new (old) time-step; and $[C_{\alpha;p}]_i$ is the concentration of species α in phase $p = l, g$ in pore i. $Q_{p;ij}$ is the phase p volumetric flow rate between pores i and j and is defined by

$$Q_{p;ij} = -\Lambda_{p;ij}[(P_{p;j} - P_{p;i}) - \rho_p G(z_j - z_i)], \quad p = l, g. \tag{22}$$

In network modeling of two-phase flow, it is common to model the phase channel conductivities $\Lambda_{p;ij}$ by variations on the Hagen–Poiseuille form to account for surface tension effects and noncircular geometry. As our code tracks s_g and not the number or size of (possibly many) individual gas bubbles that may form in a single pore, we have chosen to model $\Lambda_{p;ij}$ as a function of s_p, the latter taking its value from the upstream pore. Specifically, borrowing from the macroscopic model, we write

$$\Lambda_{p;ij} = \frac{\kappa_{ij}\kappa_{rp}A_{ij}}{\nu_p L_{ij}}, \tag{23}$$

where $\kappa_{ij} = r^2_{ij}/8$ is the intrinsic permeability and $A_{ij} = \pi r^2_{ij}$ is the cross-sectional area of the channel of radius r_{ij} and length L_{ij}, and ν_p is the fluid viscosity. $\kappa_{rp}(s_p)$ is

a "relative" permeability that we model as a function of phase saturation.

The solution of the system of Eqs. 20 and 21 gives updated values for $[m^{new}_{CO_2}]_i$ and $[m^{new}_{H_2O}]_i$. Due to numerical finite precision effects, the value of $[m^{new}_{H_2O}]_i$ may exceed C_W. In such cases, the value of $[m^{new}_{H_2O}]_i$ is reset to C_W.

3.3 Phase equilibrium update of concentrations

Following transport update of the molar concentrations, the value of the total molar concentration, the value $[m^{new}_{H_2O}]_i$ in pore i falls into one of two cases: (case 1) $[m^{new}_{H_2O}]_i = C_W$, the molar density of H_2O; or (case 2) $[m^{new}_{H_2O}]_i < C_W$. For case 1, under the assumption that $C_{H_2O;l} = C_W$, Eq. 2 has a single solution, $s_l = 1$, $s_g = 0$. In this case, all CO_2 in the pore must be dissolved in the liquid phase, hence $C_{CO_2;l} = m^{new}_{CO_2}$. As the pore has no gas phase, $C_{CO_2;g}$ and $C_{H_2O;g}$ have indeterminate value and do not couple into further computations either in this pore or its neighbors.

In case 2, Eq. 2 has solutions $0 < s_l < 1$ and $0 < s_g < 1$, i.e., the gas phase forms. Once the gas phase has formed, the concentrations of CO_2 and H_2O in the gas phase must satisfy Eqs. 1, 2, 14, and 15. The phase equilibrium calculation solves this nonlinear system for each pore by Newton's method to obtain pore values for s_l, s_g, $C_{H_2O;g}$, $C_{CO_2;l}$, and $C_{CO_2;g}$.

3.4 Stability and time-step control

For computational stability and efficiency, the propagation time, Δt, is recomputed each time-step. A propagation time interval, Δt_i, which insures that the total mass of H_2O flowing from a pore i, belonging to either category 2 or 3, does not exceed the total mass of H_2O in the pore, is estimated by

$$\Delta t_i \le \min\left(\frac{(L_{ij}+r_i+r_j)\kappa_{rl}A_{ij}}{Q_{l;ij}}, \frac{(L_{ij}+r_i+r_j)\kappa_{rg}A_{ij}}{Q_{g;ij}}\right), \tag{24}$$

where: Lij is the length and A_{ij} the cross-sectional area of the channel between pores i and j; and r_i and r_j are the radii of pores i and j. The relative permeabilities, κ_{rl} and κ_{rg}, are functions of s_l and s_g; the values for s_l and s_g are taken from the upstream pore. Condition 24 does not apply to pores of category 1. As shown in Appendix C, the stability criterion for pores of category 1 is estimated as

$$\Delta t_i \le \min(\Delta t_{i,\text{parab}}, \Delta t_{i,\text{CFL}}), \tag{25}$$

where

$$\Delta t_{i,\text{parab}} = \left|\frac{0.3 L_{i,e} V_i \nu_g \nu_l (s_{g;i} + s_{l;i}\alpha)}{n\kappa_{i,e} A_{i,e} P_g (\nu_g \kappa_{rl;i,e}\alpha + \nu_l \kappa_{rg;i,e})}\right| \tag{26}$$

and

$$\Delta t_{i,\text{CFL}} = \left|\frac{\nu_l V_i (1-\alpha)(s_{g;i} - s_{g;e})}{M_e - M_w}\right| \tag{27}$$

(Terms in Eqs. 26 and 27 are defined in Appendix C). The global propagation time, Δt, is set as the minimum over all Δt_i in Eqs. 24 and 25,

$$\Delta t = \lambda \min_i \Delta t_i, \tag{28}$$

where the factor, λ, is used to enforce stability by compensating for some of the approximations used in the derivations of Eqs. 24, 26, and 27. Numerical computation shows that a value of $\lambda = 0.9$ is necessary in our simulations.

4 Numerical results

Three test computations were performed. The first two computations were performed on a two-dimensional, regular lattice representation of a rectangular porous medium of size $3.78 \cdot 10^{-1} \times 1.7 \cdot 10^{-2} \times 3.78 \cdot 10^{-1}$ cm^3. The domain, which had a porosity of 10.86 %, contained 400 pores regularly distributed on a $20 \times 1 \times 20$ lattice. Pores were labeled with 2-D (x, z) coordinates, with the source pore labeled (0, 0). Each pore was assumed to be spherical, with radius of $5.4 \cdot 10^{-3}$ cm. The length of each channel was $1.89 \cdot 10^{-2}$ cm; the cross section area of each channel was circular, of radius $2.514 \cdot 10^{-4}$ cm.

A "quarter five-spot" flow scenario was imposed on this simulated micro-channel network; all side boundaries were sealed to flow, with input to the network occurring in the lower left corner pore and output at the upper right pore. Flow was driven by a pressure drop, the input pore was held at 1.02 bars. The outlet pore was connected through a fictitious channel to a fluid reservoir held at a pressure of 1 bar. (The cross section area of the fictitious channel was the same as that of any domain channel, while the length of the fictitious channel was the same as the radius of the outlet pore.) Under these conditions, the initial injected flow rate was $1.562 \cdot 10^{-2}$ cm s^{-1}.

The computations were performed under isothermal conditions at 50 °C, yielding the values $K_{CO_2}(T) = 22.655$ bar and $P^0_w(T) = 4.1278 \cdot 10^{-2}$ bar. With a value of $\gamma = 48.588$ dyn cm^{-1}, the characteristic value of capillary number in the 2D computations was $1.758 \cdot 10^{-5}$.

We therefore ignored the capillary pressure term P^c in the 2D network computations. The pore space was initially filled with pure water. A carbon dioxide solution, having a dissolved CO_2 concentration of $2.5132 \cdot 10^{-3}$ mol cm^{-3} (as determined from Eq. 31 using $P_l = 1.02$ bar) was injected from the source pore (0, 0). The relative permeabilities were chosen to be linear, $\kappa_{rp} = s_p$ $(p = l, g)$.

Gravity was ignored in the first computation, simulating flow in a horizontal micro-domain. In the absence of gravity, the solution obeys the symmetry of the quarter-five-spot pattern. The solubility of CO_2 throughout the domain lies in the range $2.47 \cdot 10^{-3}$ mol cm^{-3} (corresponding to a pore pressure of 1 bar) to $2.51 \cdot 10^{-3}$ mol cm^{-3} (corresponding to a pore pressure of 1.02 bar).

Gas phase first formed in pores (0, 1) and (1, 0) at 130.25 s (i.e., at $t_{130.25}$) after initial injection (Under the symmetry of the computation, the results for pores (0, 1) and (1, 0) are identical). The CO_2 solution reached the outlet pore at $t_{1,800}$. Gas phase formed in the outlet pore at $t_{9,379}$. By $t_{23,700}$, the flow had reached steady-state everywhere, with each pore occupied by gas phase. s_g values near the outlet were 3.4 %, those near the source were 0.44 %. Figure 1 presents $C_{CO_2;l}$ and s_g contour maps of the entire network at steady state; showing the symmetry of the computation.

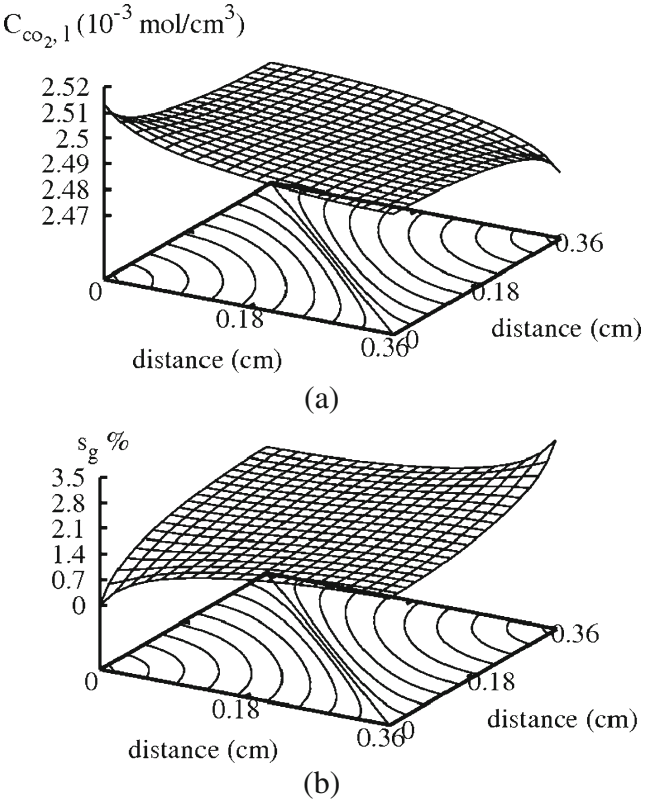

Fig. 1 Contour maps of **a** $C_{CO_2;l}$ and **b** s_g at steady state in the horizontal 2D computation

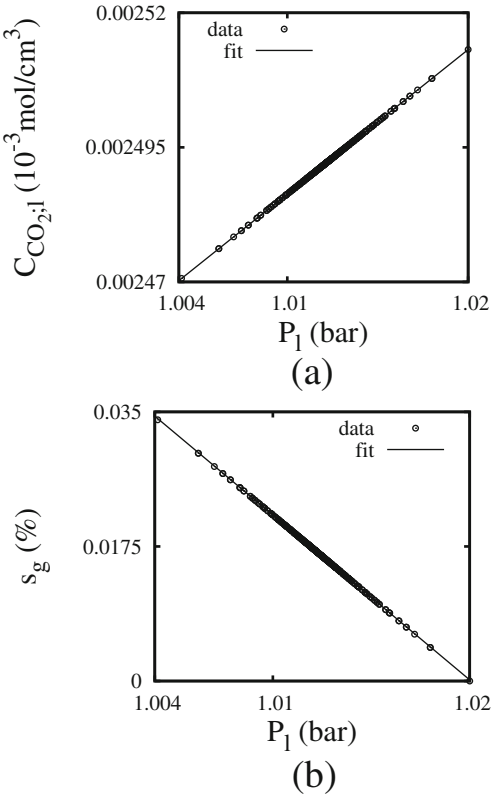

Fig. 2 **a** $C_{CO_2;l}$ and **b** s_g versus P_l for all pores in the computational region at steady-state conditions for the 2D computation with no gravity

As shown in Fig. 2, at steady state a strong linear dependency of $C_{CO_2;l}$ and s_g on P_l exists throughout the domain. The linear dependence of $C_{CO_2;l}$ with P_l can be understood as follows. Under conditions of negligible capillary pressure, Eq. 36 holds. Equation 36 can be inverted to $C_{CO_2;l} = C_{H_2O;l}(P_l - P^0_W(T))/((K_{CO_2}(T) - P_l))$. Under isothermal and liquid incompressibility assumptions, $C_{H_2O;l}$, $K_{CO_2}(T)$, and $P^0_w(T)$ are constant and $C_{CO_2;l}$ is only a function of P_l. To first order approximation, $C_{CO_2;l} \approx aP_l - b$, where $a = C_{H_2O;l}/K_{CO_2}(T) \approx 2.45 \cdot 10^{-3}$ and $b = aP^0_w(T) \approx 1.01 \cdot 10^{-4}$. A least squares fit to the data in Fig. 2a gives $a = 2.68201(2) \cdot 10^{-3}$ and $b = 2.2249(2) \cdot 10^{-4}$, where the numbers in parenthesis indicate one standard deviation error (e.g., 2.68201(2) stands for 2.68201 ± 0.00002).

For the dependence of s_g on P_l, the fit to the data in Fig. 2b gives $s_g = -2.1430(4)P_l + 2.1860(5)$. We have not, as yet, been able to explain this linear relationship analytically which, as noted below, breaks down when buoyancy effects become important.

For the computation with gravity, once the gas phase forms, buoyancy effects break the quarter-five-spot symmetry of the solution. As a consequence of buoyancy, CO_2 breakthrough occurs at later time ($t_{9,602}$) and at higher gas saturation, and steady-state conditions are reached slightly later (as buoyancy counters driving pressure to reduce the effective velocity). The loss of symmetry is demonstrated in Fig. 3a–c which compare steady-state values of P_l, $C_{CO_2;l}$, and s_g along the top and right boundaries.

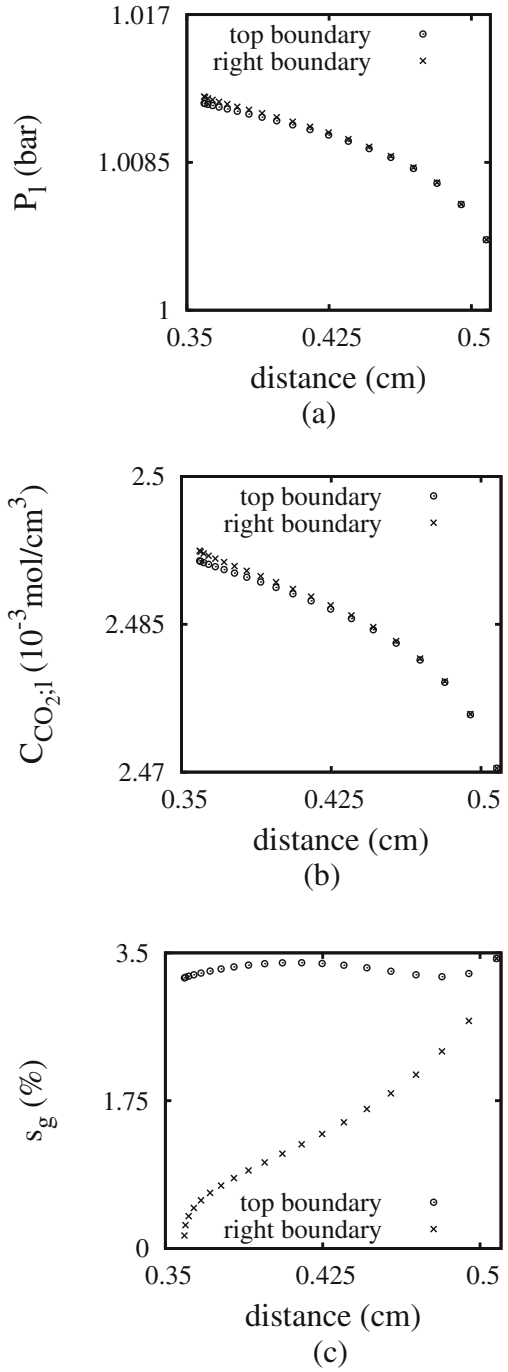

Fig. 3 **a** P_l, **b** $C_{CO_2;l}$, and **c** s_g as functions of pore position on the *top* and *right boundaries* at steady-state conditions for the 2D computation with gravity. Distance (x-axis) is measured from the source

For the computation with gravity, under steady-state conditions, the linear dependence of $C_{CO_2;l}$ on P_l is preserved (Fig. 4), with least squares fit values of $a = 2.68202(3) \cdot 10^{-3}$ and $b = 2.2250(3) \cdot 10^{-4}$, in agreement with the non-gravity case. Figure 5 examines the relationship between s_g and P_l in the computational region. Gas accumulates on the top boundary ($j = 19$) producing a nonlinear relationship between s_g and P_l (Fig. 5a). Somewhat surprisingly, the s_g - P_l relation is reasonably characterized by a linear fit, $s_g = -2.004(5)\,P_l + 2.045(5)$, for all points in the upper triangular region $i - j = p$, $p = -18, -17, \cdots, 1, 2$, $j < 19$ (Fig. 5b). The retention of approximately linear behavior in the upper triangular region with a sharp change to nonlinear behavior along the top boundary of the domain is not understood at this point. More expected is the linear to nonlinear transition behavior apparent in the s_g - P_l relationship in the lower triangular region, $i - j = q$, $q = 3, \cdots, 19$, (Fig. 5c) depending on whether pores lie on the main source-sink diagonal, or lie on the bottom or right side boundaries.

An area of interest for CO_2 sequestration is the storage capacity of a network. Table 1 contrasts the CO_2 bulk storage capacity and escape rates for this simple 2D network. There are slight differences evident, even in this small domain size, due to the influence of gravity.

The third calculation was performed on a 3D lattice representation of a rectangular porous medium of size $0.378 \times 0.378 \times 0.378\ \text{cm}^3$. The domain contained 8,000 pores regularly distributed on a $20 \times 20 \times 20$ lattice. Each pore was assumed to be spherical; pore volumes were assigned from a log-normal distribution, having

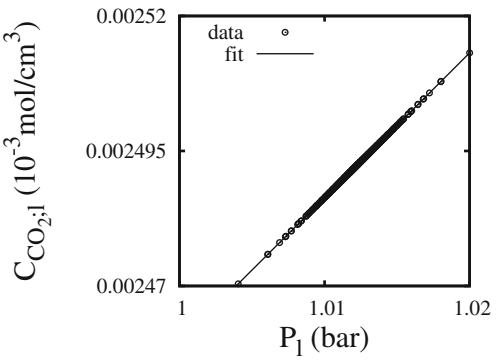

Fig. 4 $C_{CO_2;l}$ versus P_l for all pores in the computational region at steady-state conditions for the 2D computation with gravity

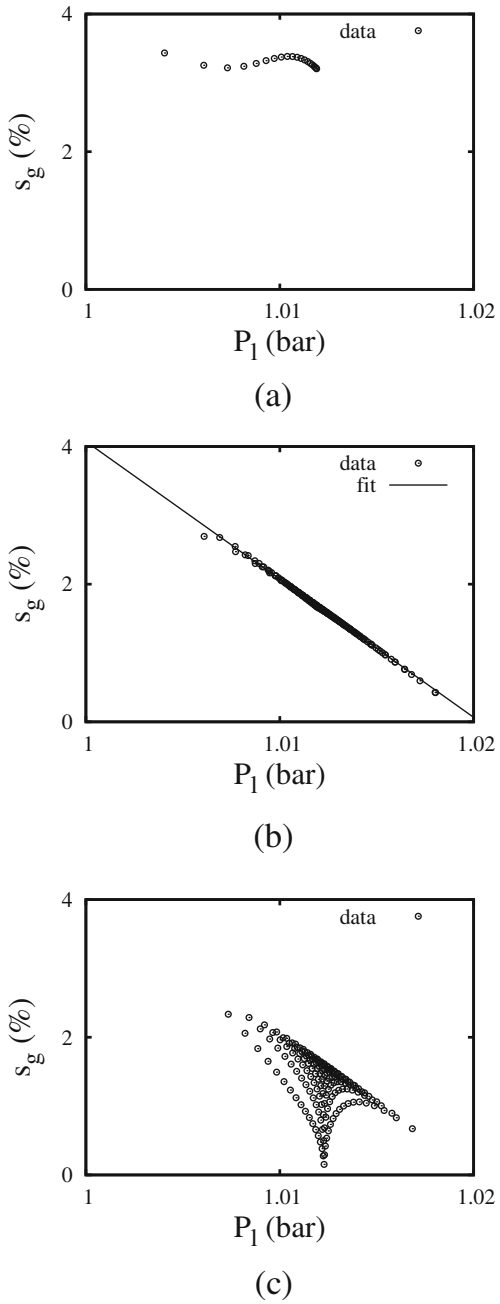

Fig. 5 s_g versus P_l for pores (i,j) satisfying **a** j = 19, **b** i − j = p, p = −18, −17, ⋯, 1, 2, j < 19, and **c** i − j = q, q = 3, ⋯, 19 at steady-state conditions for the 2D computation with gravity

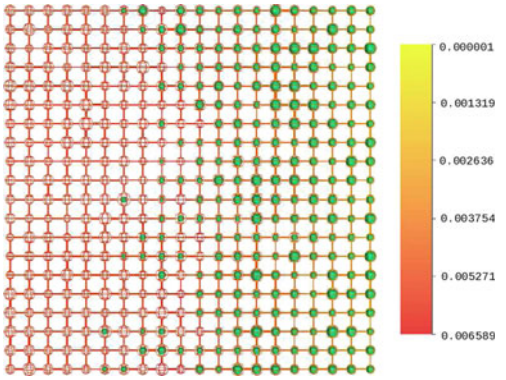

Fig. 6 $C_{CO_2;l}$ (*color scale*; mol cm^{-3}) and s_g (*solid spheres*) plotted along the central vertical plane (i,10,k) of pores (*open spheres*) and channels in the 3D computation. The volume of the solid spheres is proportional to s_g. The inlet face is to the *left*, the outlet face to the *right*

mean value $\mu_v = -6.42$ (log base 10) and standard deviation $\sigma_v = 0.51$. Since very small pores dominate the determination of the numerical time-step, the pore volume distribution was truncated, disallowing pores with volume less than $2.0 \cdot 10^{-7}$ cm^3. The resultant realization of 8,000 pores had mean pore volume of $7.6 \cdot 10^{-7}$ cm^3 and a porosity of 10 %.

The channel connecting pores i and j was assumed to be a circular pipe of radius r_{ij} and length $L_{ij} = d - r_i - r_j$ (where d is the lattice spacing and r_i and r_j are the radii of pores i and j, respectively). Following Li et al. [30], we assumed that channel's (single phase) Hagen–Poiseuille water conductivity, $\Lambda_{ij} = (\pi r_{ij}^4)/(8\nu_l L_{ij})$, obeyed a log-normal distribution correlated with the volumes V_i and V_j of pores i and j, respectively, as described in Appendix D. From each computed value of Λ_{ij}, the channel radius r_{ij} (and hence A_{ij} and κ_{ij}) were computed. Following Fourar and Lenormand [17], the relative permeabilities for the liquid and gas phase, κ_{rl} and κ_{rg}, were modeled as $\kappa_{rl} = 0.5 s_l^2(3 - s_l)$ and $\kappa_{rg} = s_g^3$, respectively.

The computation was also run at 50 °C. The pore space was filled initially with pure water. A line-drive injection was simulated. Water, fully saturated with carbon dioxide (inlet reservoir pressure 1.56 bar, CO_2 concentration $5.4795 \cdot 10^{-3}$ mol cm^{-3}), was injected at a constant flow rate, $Q = 8.14476 \cdot 10^{-5}$ cm^3 s^{-1} ($4.46285 \cdot 10^{-7}$ mol CO_2 per sec) into the network through the $x = 0$ boundary face pores. The boundary faces in the $y-$ and $z-$ directions were sealed to flow. The simulation was run for 500 s (i.e., to t_{500}).

Table 1 2D network of steady-state CO_2 storage capacity and escape rate

	Bulk s_g	Stored CO_2 (mol cm^{-3})		Escape rate (mol s^{-1})	
		Gas phase	Liquid phase	Gas phase	Liquid phase
w/o gravity	1.70 %	$6.690 \cdot 10^{-8}$	$2.662 \cdot 10^{-4}$	$2.590 \cdot 10^{-12}$	$1.502 \cdot 10^{-10}$
w gravity	1.59 %	$6.266 \cdot 10^{-8}$	$2.665 \cdot 10^{-4}$	$2.557 \cdot 10^{-12}$	$1.474 \cdot 10^{-10}$

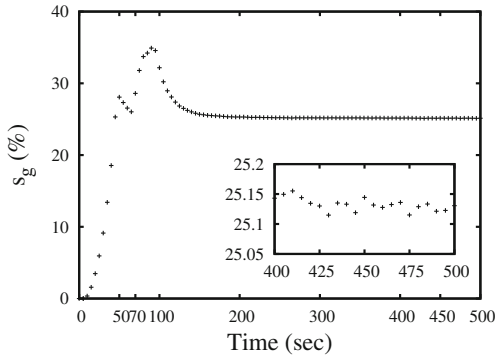

Fig. 7 Bulk s_g versus time in the 3D network. The *inset plots* shows detail over the range t_{400} to t_{500}

Figure 6 plots s_g along the central horizontal plane of pores $(i, 10, k)$ at t_{400} (the online figure plots both $C_{CO_2;l}$ and s_g, but the print figure plots only s_g). Gas bubbles predominate in pores in the outlet half of the computation. Figure 7 plots the bulk value of s_g versus time for the network. Gas phase first formed at $t_{5.25}$. At $t_{43.5}$, the gas phase reached the outlet and free gas began exiting. Figure 8 plots the amount of CO_2 in the network as a function of time in the gas and liquid phases. The inset plots in Figs. 7 and 8 indicate that the apparent steady-state condition reached after t_{400} is characterized by small oscillations.

To understand these oscillations, consider pore (10,10,15). Figure 9a–c display P_l, $C_{CO_2;l}$, and s_g versus time from t_{162} to t_{164} in this pore. At $t_{162.08}$, $C_{CO_2;l}$ ($6.194 \cdot 10^{-3}$ mol cm^{-3}) exceeded the bubble point condition and gas phase formed. During formation of the gas bubble, P_l spiked in the pore. During the expansion phase of the gas bubble, ($t_{162.08}$ to $t_{162.15}$) P_l and $C_{CO_2;l}$ declined while s_g increased. From $t_{162.15}$ to $t_{163.77}$, P_l underwent a slow decrease; s_g decreased as well (the gas phase began to dissolve). The gas phase disappeared at $t_{163.77}$; after

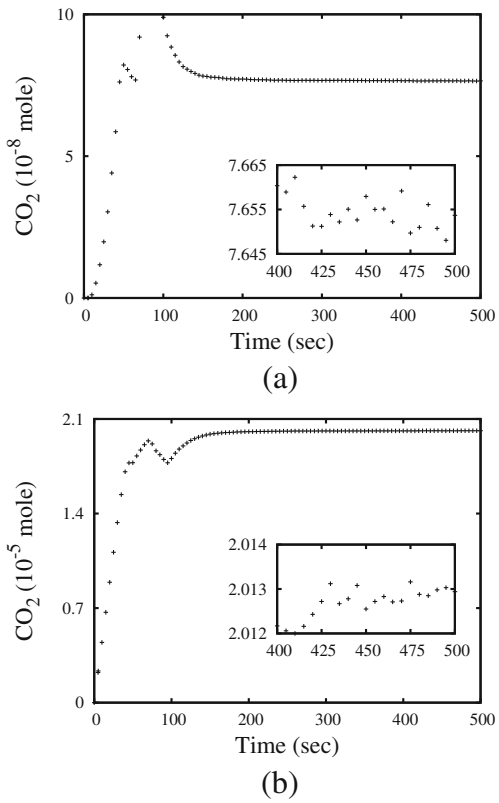

Fig. 8 Total CO_2 in the **a** gas and **b** liquid phases versus time in the 3D network. The *inset* shows detail from t_{400} to t_{500}

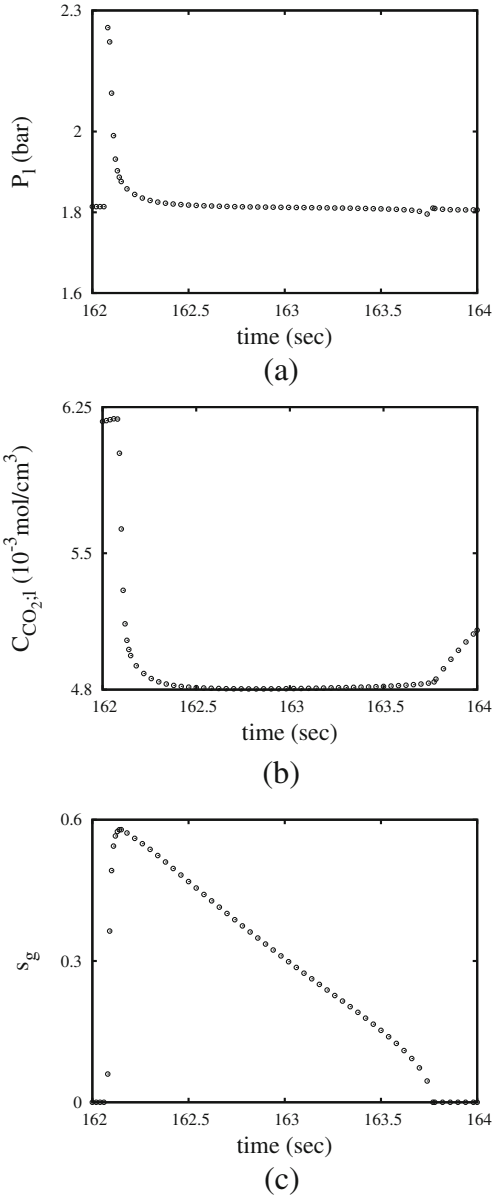

Fig. 9 **a** P_l, **b** $C_{CO_2;l}$, and **c** s_g values in pore (10,10,15) from t_{162} to t_{164} in the 3D network

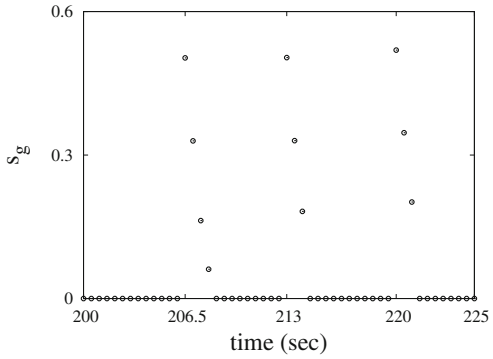

Fig. 10 s_g value in pore (10,10,15) from t_{200} to t_{225} in the 3D network

which, $C_{CO_2;l}$ quickly increased. Figure 10 displays s_g in pore (10, 10, 15) over the period t_{200}– t_{225}. The cyclic formation/disappearance of the gas phase in the pore is apparent. Between t_{400} and t_{500}, the number of pores containing gas phase varied by 0.2 % due to this cyclic behavior.

From t_{400} to t_{500}, the bulk gas saturation in the network averaged 25.12 %. This corresponded to a network bulk storage capacity for CO_2 of $3.74 \cdot 10^{-4}$ moles cm^{-3} (99.62 % in the liquid phase and 0.38 % in the gas phase). With small variation due to the cyclic behavior, CO_2 transported through the outlet face at the (injection) rate of $4.46 \cdot 10^{-7}$ mol s^{-1} but with 47 % of the exiting CO_2 in the gas phase (53 % in the liquid phase).

5 Discussion

The micro-model simulations performed here were run near bubble point pressure conditions. Despite the small size of the 2D micro-model simulated, small differences induced by buoyancy effects were detected. The linear dependence of $C_{CO_2;l}$ on P_l at steady-state conditions which holds, under the assumptions discussed, both with and without gravity provides a means of estimating CO_2 storage capacity in the liquid phase. In the no-gravity scenario, s_g is also linearly related to pressure, and thus also amenable to estimation.

In the 3D micro-model simulation, we have concentrated on bulk (core-scale) observations of the gas phase and CO_2 released by the network under bubble point conditions. While 100 % of the CO_2 entered the 3D network dissolved in the liquid phase, after 500 s of simulation time, 25 % of the void space was occupied by gas phase and 47 % of the CO_2 exiting the outlet face did so via the gaseous phase. We are still working on understanding the precise mechanism for the observed cyclic behavior of gas bubble formation in some pores. Ultimately, the behavior must reflect the fact that the stability of a gas bubble in a pore requires a sufficient concentration of dissolved CO_2 in the liquid phase which, in turn, depends on the net flux of dissolved CO_2 into the pore.

A number of improvements to this model need to be pursued. The regular rectangular networks considered here must be replaced by more geometrically realistic geologic pore networks as provided by, e.g., X-ray computed tomographic images. Diffusion of the CO_2 has been ignored; it can be included in Eq. 4 as a finite difference approximation to the standard diffusion model. The explicit nature of the current discretized numerical method results in a restrictive time step which severely increases the cpu time required to reach steady-state conditions. To handle larger networks more effectively, an implicit method needs to be considered.

The use of a relative permeability to describe competitive flow of the gas and liquid phases through channels is based upon our tracking s_g and not the number/sizes of individual gas bubbles. There are geometric forms for the phase conductivities [37, 45] that should be investigated as alternatives.

Acknowledgements This research was started when the first author was on leave from the National Pingtung University of Education, Taiwan; the university's support is gratefully acknowledged. The hospitality of the Department of Applied Mathematics and Statistics, State University of New York at Stony Brook is gratefully acknowledged. This research was partially funded by the National Sciences Council of the Republic of China under grant NSC96WFA0G00043.

Appendix A

Assume a gas bubble with radius r has formed in a CO_2 solution. Equations 14 and 15 can be rewritten

$$C_{CO_2;g} RT = K_{CO_2}(T) \frac{C_{CO_2;l}}{C_{H_2O;l} + C_{CO_2;l}}, \tag{29}$$

$$C_{H_2O;g} RT = P^0_w(T) \frac{C_{H_2O;l}}{C_{H_2O;l} + C_{CO_2;l}}, \tag{30}$$

where $K_{CO_2}(T) = P^*_{CO_2} e^{(\mu^{\ominus}_{CO_2;l}(T) - \mu^{\ominus}_{CO_2;g}(T))/RT}$ and $P^0_W(T) = P^*_{H_2O} e^{(\mu^{\ominus}_{H_2O;l}(T) - \mu^{\ominus}_{H_2O;g}(T))/RT}$. Let P^r_l be the pressure of the liquid phase surrounding the bubble. Under equilibrium conditions, from Eqs. 9 and 12, we have

$$P^r_l = P_{CO_2;g} + P_{H_2O;g} - P^c. \tag{31}$$

By Eqs. 10, 12, 29, and 30,

$$P_l^r = P_w^0(T)\frac{C_W}{(C_W + C^r_{\mathrm{CO}_2;l})} + K_{\mathrm{CO}_2;l}(T)\frac{C^r_{\mathrm{CO}_2;l}}{(C_W + C^r_{\mathrm{CO}_2;l})} - 2\gamma/r, \tag{32}$$

where $C^r_{\mathrm{CO}_2;l}$ is the CO_2 concentration dissolved in the liquid phase surrounding the bubble and γ is the surface tension of water. Solving for $C^r_{\mathrm{CO}_2;l}$ gives

$$C^r_{\mathrm{CO}_2;l} = \frac{[r(P_l^r - P_w^0(T)) + 2\gamma]C_W}{r(K_{\mathrm{CO}_2}(T) - P_l^r) - 2\gamma}. \tag{33}$$

If P_l^r is constant, $C^r_{\mathrm{CO}_2;l}$ is the solubility of CO_2 with a gas bubble (radius r) in liquid of pressure P_l^r. The derivative of Eq. 33 with respect to r,

$$\frac{dC^r_{\mathrm{CO}_2;l}}{dr} = \frac{-2\gamma C_W(K_{\mathrm{CO}_2}(T) - P_w^0(T))}{[r(K_{\mathrm{CO}_2}(T) - P_l^r) - 2\gamma]^2}, \tag{34}$$

is negative; the solubility, $C^r_{\mathrm{CO}_2;l}$, increases as the radius, r, of the bubble decreases, with $C^r_{\mathrm{CO}_2;l} \to \infty$ as $r \to 2\gamma/(K_{\mathrm{CO}_2}(T) - P_l^r)$. Thus, under a constant liquid pressure of P_l^r, a bubble with radius $2\gamma/(K_{\mathrm{CO}_2}(T) - P_l^r)$ is the minimal-sized gas bubble formed.

In our computation, we impose a minimal bubble radius of 10^{-4} cm. Therefore, the critical concentration that starts to generate a gas bubble in a pore of liquid pressure P_l is

$$C^{cr}_{\mathrm{CO}_2;l} = \frac{[10^{-4}(P_l - P_w^0(T)) + 2\gamma]C_W}{10^{-4}(K_{\mathrm{CO}_2}(T) - P_l) - 2\gamma}. \tag{35}$$

Appendix B

The evaluation of the liquid pressure for a pore which contains oversaturated carbon dioxide solution is based upon the following argument. First, assume that a sealed container, volume V, equipped with a movable piston contains gas and liquid phases comprised of the two species H_2O and CO_2. Assume the vessel is sufficiently large so that capillary effects are negligible (a planar interface exists between the gas and liquid phases).

The pressure of the gas phase is given by Eq. 12 with $P_{\mathrm{CO}_2;g}$ and $P_{\mathrm{H_2O};g}$ evaluated from Eq. 13 using Eqs. 29 and 30. Under equilibrium conditions and planar interfaces between the liquid and gas phases, the pressures of gas and of liquid phases satisfy $P_g = P_l$. The pressure of the liquid phase can then be expressed as

$$P_l = P_w^0(T)\frac{C_{\mathrm{H_2O};l}}{C_{\mathrm{H_2O};l} + C_{\mathrm{CO}_2;l}} + K_{\mathrm{CO}_2}(T)\frac{C_{\mathrm{CO}_2;l}}{C_{\mathrm{H_2O};l} + C_{\mathrm{CO}_2;l}}. \tag{36}$$

The volumes of the gas and liquid phases are $V_g = s_g V$ and $V_l = s_l V$. The total molar mass of CO_2 in the container is $m_{\mathrm{total}} = V(s_g C_{\mathrm{H_2O};g} + s_l C_{\mathrm{CO}_2;l})$. Consider moving the piston inward, forcing all of the gas phase to dissolve into the liquid. Let $C_{\mathrm{CO}_2} \equiv m_{\mathrm{total}}/V_l$. Then $C_{\mathrm{CO}_2;l} \to C_{\mathrm{CO}_2}$ as $s_g \to 0$. As P_l in Eq. 36 is a continuous function of $C_{\mathrm{CO}_2;l}$, then, as $s_g \to 0$,

$$P_l \to P_w^0(T)\frac{C_{\mathrm{H_2O};l}}{C_{\mathrm{H_2O};l} + C_{\mathrm{CO}_2}} + K_{\mathrm{CO}_2}(T)\frac{C_{\mathrm{CO}_2}}{C_{\mathrm{H_2O};l} + C_{\mathrm{CO}_2}}. \tag{37}$$

Once $s_g = 0$, if increased pressure is exerted on the piston, P_l still increases but $C_{\mathrm{CO}_2;l}$ remains at the value C_{CO_2} and the liquid becomes undersaturated solution. Therefore, P_l in Eq. 37 is the *minimum* liquid pressure required to *maintain* a dissolved CO_2 concentration of C_{CO_2}. We use Eq. 37 as the liquid pressure for any pore containing any oversaturated CO_2 solution.

Appendix C

Consider a pore in a 1-D, horizontal (gravity free) network flow model. Assume the CO_2 solution flows through the network from left to right. The left-hand channel to the pore is characterized with length L_L, cross-sectional area A_L, intrinsic permeability κ_L and relative permeabilities $\kappa_{rl;L}$ and $\kappa_{rg;L}$; the right-hand channel is characterized analogously. The relative permeability functions are evaluated using respective upstream pore saturations.

If the pore is category 1, consider Eq. 29 for the gas phase. As the water phase is assumed incompressible, $C_W \equiv C_{\mathrm{H_2O};l} = 1/18$, and, as $C_{\mathrm{CO}_2;l} \ll C_{\mathrm{H_2O};l}$, Eq. 29 can be approximated by

$$C_{\mathrm{CO}_2;g}RT \approx K_{\mathrm{CO}_2}(T)\frac{C_{\mathrm{CO}_2;l}}{C_W}. \tag{38}$$

Solving for $C_{\mathrm{CO}_2;l}$ gives

$$C_{\mathrm{CO}_2;l} \approx \alpha C_{\mathrm{CO}_2;g}, \quad \text{where } \alpha \equiv RTC_W/K_{\mathrm{CO}_2}(T). \tag{39}$$

Applying Eq. 39 to Eq. 2 gives

$$m_{\mathrm{CO}_2} = s_l\alpha C_{\mathrm{CO}_2;g} + s_g C_{\mathrm{CO}_2;g} = (s_l\alpha + s_g)C_{\mathrm{CO}_2;g}. \tag{40}$$

Applying Eqs. 39 and 40 to Eq. 21 for this pores gives,

$$\begin{aligned} &V\frac{((s_l+s_g)C_g))^{new} - ((s_l+s_g)C_g)^{old}}{\Delta t} \\ &= \left[\frac{\kappa_L A_L \kappa_{rl;L} C_{l;L}}{\nu_l}\frac{\Delta P_{l;L}}{L_L} + \frac{\kappa_L A_L \kappa_{rg;L} C_{g;L}}{\nu_g}\frac{\Delta P_{g;L}}{L_L}\right] \\ &- \left[\frac{\kappa_R A_R \kappa_{rl;R} C_{l;R}}{\nu_l}\frac{\Delta P_{l;R}}{L_R} + \frac{\kappa_R A_R \kappa_{rg;R} C_{g;R}}{\nu_g}\frac{\Delta P_{g;R}}{L_R}\right]. \end{aligned} \tag{41}$$

All concentrations in Eq. 41 refer to CO_2 concentrations (i.e., $C_{g;L} \equiv C_{\mathrm{CO}_2;g;L}$). The terms $\kappa_{rp;L}$, $C_{p;L}$, L_L, κ_L, A_L, and $\Delta P_{p;L}$ are evaluated at left quantities while the terms $\kappa_{rp;R}$, $C_{p;R}$, L_R, κ_R, A_R, and $\Delta P_{p;R}$ are evaluated at right quantities. In particular, note: $\kappa_{rp;L}$ and $C_{p;L}$ are the relative permeability and concentration of the neighboring pore to the left of this pore; $\Delta P_{p;L}$ is the pressure drop between the left (upstream) neighbor and this pore; $\kappa_{rp;R}$ and $C_{p;R}$ are the relative permeability and concentration of this pore; and $\Delta P_{p;R}$ is the pressure drop between this pore and the right (downstream) neighbor.

Since $P_l + P^c = P_g = (C_{\mathrm{CO}_2;g} + C_{\mathrm{H}_2\mathrm{O};g})RT \approx C_{\mathrm{CO}_2;g}RT$, then $\Delta P_g = RT\Delta C_{\mathrm{CO}_2;g}$ and $\Delta P_l = RT\Delta C_{\mathrm{CO}_2;g} - \Delta P^c$. Defining $L = (L_L + L_R)/2$, employing the above simplifications for ΔP_g and ΔP_l and applying Eq. 39 to the right-hand-side of Eqs. 41, 41 can be further simplified as

$$\begin{aligned} &V\frac{((s_l\alpha+s_g)C_g)^{new} - ((s_l\alpha+s_g)C_g)^{old}}{\Delta t} \\ &= \left(\frac{L\kappa_L A_L \kappa_{rl;L}}{\nu_l L_L}\frac{C_{l;L}\Delta P_{l;L}}{L} + \frac{L\kappa_L A_L \kappa_{rg;L}}{\nu_g L_L}\frac{C_{g;L}\Delta P_{g;L}}{L}\right) \\ &\quad - \left(\frac{L\kappa_R A_R \kappa_{rl;R}}{\nu_l L_R}\frac{C_{l;R}\Delta P_{l;R}}{L} + \frac{L\kappa_R A_R \kappa_{rg;R}}{\nu_g L_R}\frac{C_{g;R}\Delta P_{g;R}}{L}\right) \\ &= RTL\left[\left(\frac{\kappa_L A_L \kappa_{rl;L}\alpha}{\nu_l L_L}\frac{C_{g;L}\Delta C_{g;L}}{L} + \frac{\kappa_L A_L \kappa_{rg;L}}{\nu_g L_L}\frac{C_{g;L}\Delta C_{g;L}}{L}\right)\right. \\ &\qquad \left. - A_R\left(\frac{L\kappa_R \kappa_{rl;R}\alpha}{\nu_l L_R}\frac{C_{g;R}\Delta C_{g;R}}{L} + \frac{L\kappa_R \kappa_{rg;R}}{\nu_g L_R}\frac{C_{g;R}\Delta C_{g;R}}{L}\right)\right] \\ &\quad - L\left(\frac{\kappa_L A_L \kappa_{rl;L}\alpha}{\nu_l L_L}\frac{C_{g;L}\Delta P^c_L}{L} - \frac{\kappa_R A_R \kappa_{rl;R}\alpha}{\nu_l L_R}\frac{C_{g;R}\Delta P^c_R}{L}\right) \\ &= RTL^2\frac{\left(\frac{\kappa_L A_L}{L_L}\frac{C_{g;L}\Delta C_{g;L}\Gamma_L}{L}\right) - \left(\frac{\kappa_R A_R}{L_R}\frac{C_{g;R}\Delta C_{g;R}\Gamma_R}{L}\right)}{L} \\ &\quad - \frac{L\alpha}{\nu_l}\left(\frac{\kappa_L A_L \kappa_{rl;L}}{L_L}\frac{C_{g;L}\Delta P^c_L}{L} - \frac{\kappa_R A_R \kappa_{rl;R}}{L_R}\frac{C_{g;R}\Delta P^c_R}{L}\right) \end{aligned} \tag{42}$$

where $\Gamma_q = \frac{\kappa_{rl;q}a}{\nu_l} + \frac{\kappa_{rg;q}}{\nu_g}, q = L, R.$

After some manipulation, Eq. 42 becomes

$$\begin{aligned} &V\frac{(s_l\alpha+s_g)^{new}[C_g^{new} - C_g^{old}]}{\Delta t} \\ &\quad + V\frac{C_g^{old}[(s_l\alpha+s_g)^{new} - (s_l\alpha+s_g)^{old}]}{\Delta t} \\ &\approx RTL^2 X_L\frac{\left(\frac{C_{g;L}\Delta C_{g;L}}{L} - \frac{C_{g;R}\Delta C_{g;R}}{L}\right)}{L} \\ &\quad + RTLC_{g;R}\Delta C_{g;R}\frac{X_L - X_R}{L} - \frac{L\alpha}{\nu_l}\frac{Y_L - Y_R}{L}, \end{aligned} \tag{43}$$

where

$$\begin{aligned} X_L &= \frac{\kappa_L A_L}{L_L}\left(\frac{\kappa_{rl;L}\alpha}{\nu_l} + \frac{\kappa_{rg;L}}{\nu_g}\right), \\ X_R &= \frac{\kappa_R A_R}{L_R}\left(\frac{\kappa_{rl;R}\alpha}{\nu_l} + \frac{\kappa_{rg;R}}{\nu_g}\right), \\ Y_L &= \frac{\kappa_L A_L \kappa_{rl;L} C_{g;L}\Delta P^c_L}{L_L}, \\ Y_R &= \frac{\kappa_R A_R \kappa_{rl;R} C_{g;R}\Delta P^c_R}{L_R}. \end{aligned}$$

Eq. 43 can be viewed as a linear combination of the two equations

$$\begin{aligned} &V\frac{(s_l\alpha+s_g)^{new}(C_g^{new} - C_g^{old})}{\Delta t} \\ &\approx RTL^2 X_L\frac{\frac{C_{g;L}\Delta C_{g;L}}{L} - \frac{C_{g;R}\Delta C_{g;R}}{L}}{L}, \end{aligned} \tag{44}$$

and

$$\begin{aligned} &V\frac{C_g^{old}[(s_l\alpha+s_g)^{new} - (s_l\alpha+s_g)^{old}]}{\Delta t} \\ &\approx RTL^2\frac{C_{g;R}\Delta C_{g;R}}{L}\frac{X_L - X_R}{L} - \frac{L\alpha}{\nu_l}\frac{Y_L - Y_R}{L}, \end{aligned} \tag{45}$$

Replacing s_l with $1 - s_g$, recognizing that $C^{old}_{\mathrm{CO}_2;g}$ and $C_{g;R}$ are identical notations, and employing some trivial manipulation, Eq. 45 can be rewritten as

$$\begin{aligned} &V(1-\alpha)\frac{s_g^{new} - s_g^{old}}{\Delta t} \\ &\approx \left(RTL\Delta C_{g;R}\frac{X_L - X_R}{s_{g;L} - s_{g;R}} - \frac{L\alpha}{\nu_l}\frac{Y_L - Y_R}{s_{g;L} - s_{g;R}}\right)\frac{s_{g;L} - s_{g;R}}{L} \\ &\approx L\frac{(\nu_l\Delta P_{g;R}X_L - \alpha Y_L) - (\nu_l\Delta P_{g;R}X_R - \alpha Y_R)}{\nu_l(s_{g;L} - s_{g;R})}\frac{s_{g;L} - s_{g;R}}{L}. \end{aligned} \tag{46}$$

Equation 44 is a discrete approximation to the parabolic equation

$$V(s_l\alpha + s_g)\frac{\partial C_g}{\partial t} \approx -RTL^2\frac{\kappa_L A_L}{L_L}\left(\frac{\kappa_{rl;L}\alpha}{\nu_l} + \frac{\kappa_{rg;L}}{\nu_g}\right)\frac{\partial\left(C_g\frac{\partial C_g}{\partial L}\right)}{\partial L}. \quad (47)$$

Equation 47 is a second-order parabolic equation. As our numerical discretization is an explicit method, the stability criterion for Eq. 47 satisfies

$$\left|\Delta t_{\text{parab}}\frac{\kappa_L A_L P_g(\nu_g\kappa_{rl;L}\alpha + \nu_l\kappa_{rg;L})}{(s_g + s_l\alpha)V\nu_g\nu_l L_L}\right| < c, \quad (48)$$

for some constant, c. Based upon several 1-D computations, varying the flow rate over five orders of magnitude, we find empirically that $c \approx 0.3$. Thus,

$$\Delta t_{\text{parab}} \le \left|\frac{0.3L_L V\nu_g\nu_l(s_g + s_l\alpha)}{\kappa_L A_L P_{g;L}(\nu_g\kappa_{rl;L}\alpha + \nu_l\kappa_{rg;L})}\right|. \quad (49)$$

Equation 46 is a discrete approximation to the first-order hyperbolic equation

$$(1-\alpha)V\frac{\partial s_g}{\partial t} = -L\frac{(\nu_l\Delta P_{g;R}X_L - \alpha Y_L) - (\nu_l\Delta P_{g;R}X_R - \alpha Y_R)}{\nu_l(s_{g;L} - s_{g;R})}\frac{\partial s_g}{\partial L}. \quad (50)$$

The stability criterion of Eq. 50 follows the CFL condition

$$\Delta t_{\text{CFL}} \le \left|\frac{\nu_l V(1-\alpha)(s_{g;R} - s_{g;L})}{(\nu_l\Delta P_{g;R}X_L - \alpha Y_L) - (\nu_l\Delta P_{g;R}X_R - \alpha Y_R)}\right|. \quad (51)$$

Since the propagation step time must satisfy both Eqs. 49 and 51,

$$\Delta t = \min(\Delta t_{\text{parab}}, \Delta t_{\text{CFL}}). \quad (52)$$

For the stability of 2D or 3D network calculations, assume the carbon dioxide solution flows into pore i through n channels and flows out from pore i through m channels. Let $\Omega_{in;i,j}$ $(j = 1, 2, \cdots, n)$ be the total concentration of CO_2 flowing from pore j into pore i and let $\Omega_{out;i,k}$ $(k = 1, 2, \cdots, m)$ be the total concentration of CO_2 flowing out from pore i into pore k. Let $C_{p;j}$ and $P_{p;j}$ be the CO_2 concentration and pressure of phase p $(p = l, g)$ in pore j respectively; κ_{rp}, ρ_p and ν_p be the relative permeability, density, and viscosity of phase p; κ, A_{ij}, and L_{ij} be the intrinsic permeability, the cross-sectional area, and the length of the channel between pore i and pore j; z_j be the pore center position in the vertical direction; and G be the gravitational acceleration. Similar to Eq. 22,

$$\Omega_{in;i,j} = -\left(\frac{C_{l;j}\kappa_{ij}\kappa_{rl}}{\nu_l}A_{ij}\frac{(P_{l;i} - P_{l;j}) - \rho_l G(z_i - z_j)}{L_{ij}} + \frac{C_{g;j}\kappa_{ij}\kappa_{rg}}{\nu_g}A_{ij}\frac{(P_{g;i} - P_{g;j}) - \rho_g G(z_i - z_j)}{L_{ij}}\right), \quad (53)$$

where $P_{p;j} > P_{p;i}$ $(p = l, g)$ and

$$\Omega_{out;i,k} = -\left(\frac{C_{l;i}\kappa_{ik}\kappa_{rl}}{\nu_l}A_{ik}\frac{(P_{l;i} - P_{l;k}) - \rho_l G(z_i - z_k)}{L_{ik}} + \frac{C_{g;i}\kappa_{ik}\kappa_{rg}}{\nu_g}A_{ik}\frac{(P_{g;i} - P_{g;k}) - \rho_g G(z_i - z_k)}{L_{ik}}\right), \quad (54)$$

where $P_{p;k} < P_{p;i}$ $(p = l, g)$.

Let e be the pore such that $\Omega_{in;i,e} = \max_{j=1,\cdots,n}\Omega_{in;i,j}$ and w be the pore such that $\Omega_{out;i,w} = \min_{k=1,\cdots,m}\Omega_{out;i,k}$. From Eq. 21,

$$V_i\frac{[m_{CO_2}^{new}]_i - [m_{CO_2}^{old}]_i}{\Delta t} = \sum_{j=1}^{n}\Omega_{in;i,j} + \sum_{j=1}^{m}\Omega_{out;i,j}. \quad (55)$$

Consider the maximum CO_2 mass change,

$$V_i\frac{[m_{CO_2}^{new}]_i - [m_{CO_2}^{old}]_i}{\Delta t} = (n\Omega_{in;i,e} + m\Omega_{out;i,w}) = \left[\frac{n\kappa_{i,e}A_{i,e}\kappa_{rl;i,e}C_{l;e}}{\nu_l}\frac{\Delta P_{l;i,e}}{L_{i,e}} + \frac{n\kappa_{i,e}A_{i,e}\kappa_{rg;i,e}C_{g;e}}{\nu_g}\frac{\Delta P_{g;i,e}}{L_{i,e}}\right] - \left[\frac{m\kappa_{i,w}A_{i,w}\kappa_{rl;i,w}C_{l;w}}{\nu_l}\frac{\Delta P_{l;i,w}}{L_{i,w}} + \frac{m\kappa_{i,w}A_{i,w}\kappa_{rg;i,w}C_{g;w}}{\nu_g}\frac{\Delta P_{g;i,w}}{L_{i,w}}\right], \quad (56)$$

where $\kappa_{rp;i,e}$,$\kappa_{rp;i,w}$ $(p = l, g)$ are the relative permeabilities for phase p flowing through the channels connecting pores i to e and i to w, and $\Delta P_{p;i,e}$, $\Delta P_{p;i,w}$ are the pressure drops for phase p between pores i, e and i, w. Since $\sum_{j=1}^{n}\Omega_{in;i,j} + \sum_{k=1}^{m}\Omega_{out;i,k} \le n\Omega_{in;i,e} + m\Omega_{out;i,w}$, any Δt that is stable for Eq. 56 is also stable for Eq. 55. Equation 56 is an effective 1D statement; from Eqs. 49, 51, and 53 we infer

$$\Delta t_{\text{parab}} \le \left|\frac{0.3L_{i,e}V_i\nu_g\nu_l(s_{g;i} + s_{l;i}\alpha)}{n\kappa_{i,e}A_{i,e}P_g(\nu_g\kappa_{rl;i,e}\alpha + \nu_l\kappa_{rg;i,e})}\right|, \quad (57)$$

$$\Delta t_{\mathrm{CFL}} \leq \left| \frac{\nu_l V_i (1-\alpha)(s_{g;i} - s_{g;e})}{M_e - M_w} \right|, \tag{58}$$

and

$$\Delta t = \min(\Delta t_{\mathrm{parab}}, \Delta t_{\mathrm{CFL}}), \tag{59}$$

where

$$M_e = \nu_l \Delta P_{g;i,w} X_e - C_{g;e} \Delta P^c_{i,e} Y_e,$$
$$M_w = \nu_l \Delta P_{g;i,w} X_w - C_{g;i} \Delta P^c_{i,w} Y_w,$$
$$X_e = \frac{n \kappa_{i,e} A_{i,e}}{L_{i,e}} \left(\frac{\kappa_{rl;i,e} \alpha}{\nu_l} + \frac{\kappa_{rg;i,e}}{\nu_g} \right),$$
$$X_w = \frac{m \kappa_{i,w} A_{i,w}}{L_{i,w}} \left(\frac{\kappa_{rl;i,w} \alpha}{\nu_l} + \frac{\kappa_{rg;i,w}}{\nu_g} \right),$$
$$Y_e = \frac{\alpha n \kappa_{i,e} A_{i,e} \kappa_{rl;i,e}}{\nu_l L_{i,e}} \quad \text{and} \quad Y_w = \frac{\alpha m \kappa_{i,w} A_{i,w} \kappa_{rl;i,w}}{\nu_l L_{i,w}}.$$

Appendix D

Let $X_{ij} \equiv \log \Lambda_{ij}$. X_{ij} was sampled from a correlated normal distribution having mean $\mu_{\mathrm{X}_{ij}}$ and standard deviation $\sigma_{\mathrm{X}_{ij}}$ given by

$$\mu_{\mathrm{X}_{ij}} = \mu_{\mathrm{X}} + \rho \frac{\sigma_{\mathrm{X}}}{\sigma_{\mathrm{Y}}} (Y_{ij} - \mu_{\mathrm{Y}}), \quad \sigma^2_{\mathrm{X}_{ij}} = \sigma^2_{\mathrm{X}} (1 - \rho^2). \tag{60}$$

Here, $Y_{ij} \stackrel{\mathrm{def}}{=} \log V_i + \log V_j$ is a Gaussian-sum random variable having mean value $\mu_{\mathrm{Y}} = 2\mu_{\mathrm{V}}$ and standard deviation $\sigma_{\mathrm{Y}} = \sqrt{2}\sigma_{\mathrm{V}}$, and ρ is a correlation coefficient. Values chosen for the free variables were $\mu_{\mathrm{X}} = -10.1$, $\sigma_{\mathrm{X}} = 1.0$, and $\rho = 0.9$.

References

1. Aker, E., Maloy, K.J. Hansen, A., Batrouni, G.G.: A two-dimensional network simulator for two-phase flow in porous media. Trans. Porous Media **32**, 163–186 (1998)
2. Atkins, P., Depaula, J.: Atkins Physical Chemistry, 8th edn, pp. 996–997. Oxford University Press (2006)
3. Albritton, D.L., Meira Filho, L.G.: Technical summary, Climate change 2001: The scientific basis; contribution of working group I to the third assessment report of the intergovernmental panel on climate change. Geneva, Switzerland (2001)
4. Bachu, S.: Geologic sequestration of anthropogenic carbon dioxide: applicability and current issues. In: Gerhard, L.C., Harrison, W.E., Hanson, B.M. (eds.) Geological Perspectives of Global Climate Change. pp. 285–303. American Association of Petroleum Geologists, Tulsa, OK (2001)
5. Bachu, S.: Sequestration of CO_2 in geological media in response to climate change: roadmap for site selection using the transform of geologic space into the CO_2-phase space. Energy Convers. Manag. **43**, 87–102 (2002)
6. Bachu, S., Gunter, W.D., Perkins, E.H.: Aquifer disposal of CO_2: hydrodynamic and mineral trapping. Energy Convers. Manag. **35**, 267–279 (1994)
7. Bergman, P.D., Winter, E.M.: Disposal of carbon dioxide in aquifers in the US. Energy Convers. Manag. **36**, 523–526 (1995)
8. Blunt, M.J.: Flow in porous media–pore-network models and multiphase flow. Curr. Opin. Colloid Interface Sci. **6**, 197–207 (2001)
9. Blunt, M., King, P.: Relative permeabilities from two- and three-dimensional pore-scale network modelling. Trans. Porous Media **6**, 407–433 (1991)
10. Bruant, R.G., Guswa, Jr., A.J., Celia, M.A., Peters, C.A.: Safe storage of carbon dioxide in deep saline aquifers. Environ. Sci. Technol. **36**, 240A–245A (2002)
11. Celia, M.A., Reeves, P.C., Ferrand, L.A.: Recent advances in pore scale models for multiphase flow in porous-media. Rev. Geophys. **33**, 1049–1057 (1995)
12. Celia, M.A., Nordbotten, J.M.: Practical modeling approaches for geological storage of carbon dioxide. Ground Water **47**:627–638 (2009)
13. Dahle, H.K., Celia, M.A.: A dynamic network model for two-phase immiscible flow. Comput. Geosci. **3**, 1–22 (1999)
14. Davison, J., Freund, P., Smith, A.: Putting carbon back in the ground. IEA Greenhouse Gas R&D Programme, Gloucestershire, UK (2001)
15. Falkowski, P., Scholes, R.J., Boyle, E., Canadell, J., Candeld, D., Elser, J., Gruber, N., Hibbard, K., Hogberg, P., Under, S., Mackenzie, F.T., Moore, B.I., Pedersen, T., Rosenthal, Y., Seitzinger, S., Smetacek, V., Steffen, W.: The global carbon cycle: a test of our knowledge of earth as a system. Science **290**, 291–296 (2000)
16. Fatt, I.: The network model of porous media: I. capillary characteristics. Pet. Trans. A1ME **207**, 144–159 (1956)
17. Fourar, M., Lenormand, R.: A viscous coupling model for relative permeabilities in fractures. SPE 49006, paper presented at the SPE Annual Technical Conference and Exhibition. New Orleans, LA, USA (1998)
18. Freeth, S.J., Kay, R.L.F.: The Lake Nyos gas disaster. Nature **325**, 104–105 (1987)
19. Gielen, T., Hassanizadeh, S.M., Leijnse, A., Nordhaug, H.F.: Dynamic effects in multiphase flow: a pore-scale network approach. In: Das, D.B., Hassanizadeh, S.M. (eds.) Upscaling Multiphase Flow in Porous Media from Pore to Core and Beyond, pp. 217–236. Springer, Dorcrecht, The Netherlands (2005)
20. Gupta, N., Sass, B., Sminchak, J., Naymik, T.: Hydrodynamics of CO_2 disposal in a deep saline formation in the midwestern United States. In: Riemer, P., Eliasson, B., Wokaun, A. (eds.) Greenhouse Gas Control Technologies, pp. 157–162. Elsevier Science Ltd (1999)
21. Gvirtzman, H., Roberts, P.V.: Pore scale spatial analysis of two immiscible fluids in porous media. Water Resour. Res. **22**, 1165–1176 (1991)
22. Hassanizadeh, S.M., Celia, M.A., Dahle, H.K.: Dynamic effect in the capillary pressure–saturation relationship and its impacts on unsaturated flow. Vadose Zone J. **1**, 38–57 (2002)
23. Herzog, H.J.: What future for carbon capture and sequestration? Environ. Sci. Technol. **35**, 148A–153A (2001)
24. Holloway, S.: An overview of the underground disposal of carbon dioxide. Energy Convers. Manag. **35**, S193–S198 (1997)
25. Jackson, M.D., Valvatne, P.H., Blunt, M.J.: Prediction of wettability variation within an oil/water transition zone and its impact on production. SPEJ **10**, 185–195 (2005)

26. Kim, D., Peters, C.A., Lindquist, W.B.: Up-scaling geochemical reaction rates accompanying acidic CO_2-saturated brine flow in sandstone aquifers. Water Resour. Res. **47**, W01505 (2011)
27. Kling, G.W., Clarx, M.A., Compton, H.R., Devine, J.D., Evans, W.C., Humphrey, A.M., Koenigsberg, E.J., Lockwood, J.P., Tutrle, M.L., Wagner, G.N.: The 1986 Lake Nyos gas disaster in Cameroon, West Africa. Science **236**, 169–175 (1987)
28. Knackstedt, M.A., Sheppard, A.P., Sahimi, M.: Pore network modeling of two-phase flow in porous rock: the effect of corrected heterogeneity. Adv. Water Resour. **24**, 257–277 (2001)
29. Le Gallo, Y., Bildstein, O., Brosse, E.: Coupled reaction-flow modeling of diagenetic changes in reservoir permeability, porosity and mineral compositions. J. Hydrol. **209**, 366–388 (1998)
30. Li, L., Peters, C.A., Celia, M.A.: Upscaling geochemical reaction rates using pore-scale network modeling. Adv. Water Resour. **29**, 1351–1370 (2006)
31. Li, L., Peters, C.A., Celia, M.A.: Effects of mineral spatial distribution on reaction rates in porous media. Water Resour. Res. **43**, W01419 (2007)
32. Li, L., Peters, C.A., Celia, M.A.: Applicability of averaged concentrations in determining geochemical reaction rates in heterogeneous porous media. Am. J. Sci. **307**, 1146–1166 (2007)
33. Nordbotten, J.M., Kavetski, D., Celia, M.A.,Bachu, S.: Model for CO_2 leakage including multiple geological layers and multiple leaky wells. Environ. Sci. Technol. **43**, 743–749 (2009)
34. Olbricht, W.L.: Pore-scale prototypes of multiphase flow in porous media. Annu. Rev. Fluid Mech. **28**, 187–213 (1996)
35. Pacala, S., Socolow, R.: Stabilization wedges: solving the climate problem for the next 50 years with current technologies. Science **305**, 968–972 (2004)
36. Pereira, G.G., Pinczewski, W.V., Chan, D.Y.C., Paterson, L., Oren, P.E.: Pore-scale network model for drainage dominated three-phase flow in porous media. Trans. Porous Media **24**, 167–201 (1996)
37. Ransohoff, T.C., Radke, C.J.: Laminar flow of a wetting liquid along the corners of a predominantly gas-occupied noncircular pore. J. Colloid Interface Sci. **121**, 392–401 (1988)
38. Schlumberger: Eclipse 100/300 Reference manual and technical manual (2006)
39. Schlumberger: Eclipse technical description 2007.1 (2007)
40. Sholokhova, Y., Kim, D., Lindquist, W.B.: Network flow modeling via lattice-Boltzmann based channel conductance. Adv. Water Resour. **32**, 205–212 (2009)
41. Sinha, P.K., Wang, C.Y.: Pore-network modeling of liquid water transport in gas diffusion layer of a polymer electrolyte fuel cell. Electrochim. Acta **52**, 7936–7945 (2007)
42. Sok, R.M., Knackstedt, A., Sheppard, A.P., Pinczewski, W.V., Lindquist, W.B., Venkatarangan, A., Paterson, L.: Direct and stochastic generation of network models from tomographic images: effect of topology on residual saturations. Trans. Porous Media **46**, 345–372 (2002)
43. Stark, J., Manga, M.: The motion of long bubbles in a network of tubes. Trans. Porous Media **40**, 201–218 (2000)
44. Wigley, T.M.L., Richels, R., Edmonds, J.A.: Economic and environmental choices in the stabilization of atmospheric CO_2 concentrations. Nature **379**, 240–243 (1996)
45. Zhou, D., Blunt, M.J., Orr, F.M.: Hydrocarbon drainage along corners of noncircular capillaries. J. Colloid Interface Sci. **187**, 11–21 (1997)